Extrapolating Glioma Invasion Margin in Brain Magnetic Resonance Images: Suggesting New Irradiation Margins

Ender Konukoglu, Olivier Clatz, Pierre-Yves Bondiau, Hervé Delingette, Nicholas Ayache

Extrapolating Glioma Invasion Margin in Brain Magnetic Resonance Images: Suggesting New Irradiation Margins

Ender Konukoglu[a], *,[1] Olivier Clatz[a], Pierre-Yves Bondiau[b], Hervé Delingette[a] and Nicholas Ayache[a]

[a] *Asclepios Research Project, INRIA Sophia Antipolis, France*
[b] *Centre Antoine Lacassagne, Nice, France*

Abstract

Radiotherapy for brain glioma treatment relies on magnetic resonance (MR) and computed tomography (CT) images. These images provide information on the spatial extent of the tumor, but can only visualize parts of the tumor where cancerous cells are dense enough, masking the low density infiltration. In radiotherapy, a 2 cm constant margin around the tumor is taken to account for this uncertainty. This approach however, does not consider the growth dynamics of gliomas, particularly the differential motility of tumor cells in the white and in the gray matter. In this article, we propose a novel method for estimating the full extent of the tumor infiltration starting from its visible mass in the patients' MR images. This estimation problem is a time independent problem where we do not have information about the temporal evolution of the pathology nor its initial conditions. Based on the reaction-diffusion models widely used in the literature, we derive a method to solve this extrapolation problem. Later, we use this formulation to tailor new tumor specific variable irradiation margins. We perform geometrical comparisons between the conventional constant and the proposed variable margins through determining the amount of targeted tumor cells and healthy tissue in the case of synthetic tumors. Results of these experiments suggest that the variable margin could be more effective at targeting cancerous cells and preserving healthy tissue.

* Email: ender.konukoglu@gmail.com, Tel:+33 (0)492 387 927 , Address: 2004 Route des Lucioles, 06902 Sophia Antipolis, France

[1] This work has been partly supported by the European Health-e-Child project (IST-2004-027749), by the CompuTumor project (http://www-sop.inria.fr/asclepios/projects/boston/) and by Microsoft Research Cambridge. The present contact for the corresponding author is: Tel: +44 1223 479 884, Address: 7 J J Thomson Avenue, Cambridge, CB3 0FB United Kingdom

1 Introduction

Brain gliomas form the major class of tumors in the central nervous system, [44,29]. Among them, high grade ones remain incurable despite the state-of-the-art therapy, and patients have an average life expectancy of 1 year, [40]. For diagnosis and therapy of gliomas, clinicians rely on medical images, such as Magnetic Resonance (MR) and Computed Tomography (CT). These images show the dense part of the tumor. However, with the current technology they are not able to expose the low density infiltration as different studies show the presence of tumor cells beyond the radiological signal [45,41,5,48]. This poses a problem for the experts in outlining the whole tumor and in understanding its extent. Figure 1 illustrates this observability problem. In radiotherapy the invisible low density infiltration is addressed by outlining the tumor volume (more precisely the clinical target volume CTV2) and assuming the whole tumor infiltration would be contained within a 2 cm constant margin around that volume [32,20]. The irradiation region is constructed accordingly. This approach however, does not take into account the infiltration dynamics of gliomas, particularly the higher motility of tumor cells in the white matter compared to the gray matter [14]. As a result, the irradiation region ignoring these dynamics would not reach the full extent of the tumor infiltration in the white matter and irradiate gray matter where probability of finding tumor cells would be very low. Mathematical tumor growth models can offer solutions to this problem by integrating clinical information and theoretical knowledge about tumor cell dynamics [40,42,35,36]. In this respect, here we describe a formulation based on medical images, which aims to solve the problem of estimating tumor cell density distribution beyond the visible part in the image (low density infiltration) for gliomas. It uses the anatomical MR images and the diffusion tensor imaging (DTI) to suggest irradiation margins taking into account the inhomogeneity of the tumor invasion.

Over the last decade researchers proposed a variety of different tumor growth models. These different approaches can be coarsely classified into two groups, microscopic and macroscopic models. Microscopic models try to describe the progression of the tumor at the cellular level in terms of interactions between individual cells and their surrounding [9,28,11,19,17,1,13,31,25,7,6,4,3]. These models are detailed, discrete and aim to capture the stochastic nature of tumor growth. However, they often include microscopic parameters that are not observable from medical images. This makes them harder to adapt to specific patient cases. Macroscopic models on the other hand, describe the average behavior of tumor cells and model the evolution of local tumor cell densities rather than individual cells [39,8,18,9,16,45,10,13,26,37]. Therefore, it is harder for them to capture the stochastic characteristic of tumor growth. On the other hand, they usually have fewer equations and parameters which can be identified from medical images making macroscopic models easier to adapt

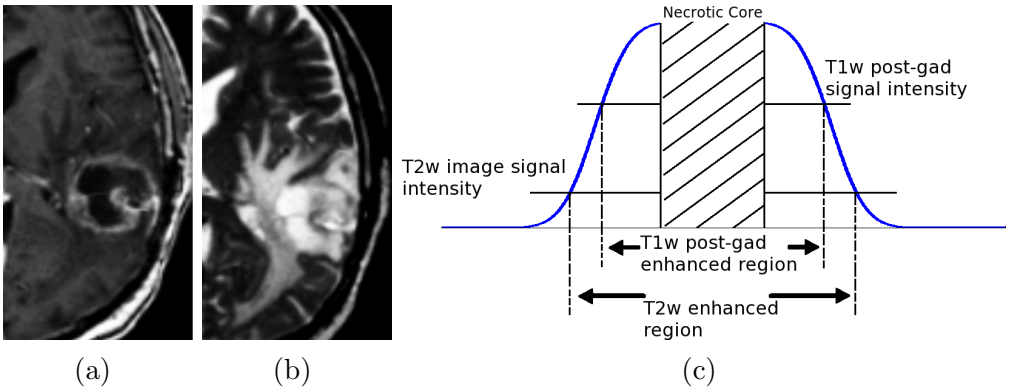

Fig. 1. (a) T1-weighted post-gadolinium and (b) T2-weighted MR images of a high grade glioma. Two clinically important volumes, the bulk tumor (CTV1) and the infiltrated edema (CTV2), are the enhanced regions in Figures (a) and (b) respectively. (c) Hypothetical distribution of tumor cell density is given by the smooth curve. Tumor distribution extends beyond the enhanced region and cells can be found outside the radiological signal.

to specific patient data.

Most of the macroscopic models, [39,8,18,16,37], are based on the reaction-diffusion formalism Murray introduced in the early 1990 and later formulated as a conservation equation [27,40]. This formalism uses the general class of partial differential equations (PDEs) called the reaction-diffusion and reaction-diffusion-advection type. They describe the temporal change of tumor cell densities at different locations in the brain through diffusion, migration and mitosis of tumor cells. The complexity of these models vary depending on the number of factors they take into account. In this work we derive our method starting from the reaction-diffusion equations. Since we focus on clinically available data (i.e. medical images), we choose to base our method on simpler reaction-diffusion models as given in [39,8,18]. The number of parameters for these models are few and can be directly related to the available clinical data such as the anatomical MRI and the DTI.

The literature on predicting irradiation margins on medical images using automatic methods is rather limited. In [21], Kaspari *et al.* used artificial neural networks to model statistically the way the radiotherapist constructs the irradiation margin. In their work they do not include the growth dynamics of gliomas. Zizzari *et al.* started from the same framework and included mathematical growth models in their prediction of the irradiation volume [49]. They use their model to predict further growth of the tumor and then use this prediction to construct the irradiation margins through artificial neural networks. However, they do not focus on the spatial distribution of tumor cells at a given time and they do not include the differential motility of glioma cells in different tissues. In [40], Swanson *et al.* also focus on the problem of limited visualization of gliomas. For virtual tumors grown by reaction-diffusion mod-

els, they compare the visible part of the tumor with the extent of the invisible infiltration. This work is important in demonstrating the visualization problem for brain gliomas. However, their work does not provide concrete methods to solve this problem for patient images.

In this article, we propose a formulation to extrapolate the tumor cell density distribution of diffusive gliomas beyond their visible mass in MR images taking into account the growth tendencies of the tumor. In deriving the formulation we start from the reaction-diffusion type growth models as given in [8,18,40]. Directly applying these models to solve the mentioned problem poses several difficulties. First, reaction-diffusion models require the knowledge of tumor cell densities at every point in the brain while in reality only CTV1 and/or CTV2 contours are observable in the images. In addition, reaction-diffusion models describe the *temporal evolution* of tumor cell density distribution, however, the problem we are tackling is *static*, dealing with the distribution of tumor cell density at a *single time instance*. We use asymptotic approximations to overcome these difficulties and derive a static formulation that uses the information in the images. The proposed method starts from the delineation of the tumor (manual delineation or automatic segmentation) and constructs an approximation for the low density infiltration taking into account the underlying tissue characteristics by using anatomical and diffusion tensor images. With such a formulation, we aim to construct irradiation margins that would be more efficient in targeting tumor cells and reducing the irradiation of healthy brain tissues.

In Section 2, we explain the reaction-diffusion type models in detail and derive our formulation for extrapolating low density infiltration using a single image. In Section 3 we assess the quality of the approximation constructed by the proposed formulation using virtually grown tumors. Following this, we use our formulation to construct a variable irradiation margin. We compare these margins to the conventionally used constant ones in terms of number of tumor cells and volume of healthy tissue targeted in the case of synthetic tumors. In Section 4 we conclude by summarizing the work with our results and provide future directions.

2 Method

Before detailing the proposed method let us mathematically formulate the problem we solve and state its difference from modeling the temporal evolution of the tumor. Let us denote the smooth tumor cell density distribution shown in Figure 1(c) by $u(\mathbf{x}, t)$, where $\mathbf{x}$ denotes the location in the brain and t is the time. In terms of u, the imaging process of gliomas can be modeled with

a simple Heaviside function as done in previous works [40,45]:

$$Im(u(\mathbf{x},t)) = \begin{cases} 1 \text{ if } u \geq u_0 \\ 0 \text{ if } u < u_0 \end{cases} \quad (1)$$

where Im is the imaging function and u_0 is the detection threshold, which hypothetically depends on the imaging modality. A detection threshold u_0 is given for CT images in [45] ($u_0 = 0.4$) and based on the coherence of observations obtained from MR images, radiologists assume a similar threshold for T1w post-gad images. For the regions enhanced in the T2w and the FLAIR images a lower value of u_0 is assumed in the literature [42]. However, this value is purely hypothetical. The exact values of these thresholds or even the form of the imaging function remain as an open problem. In this setting, the problem of extrapolating the cell density distribution of a tumor beyond its visible part in the image ($u < u_0$), starting from its delineation, can be described as constructing an approximation

$$\tilde{u}(\mathbf{x}) \approx u(\mathbf{x}, T_0) \; \forall \; \mathbf{x} \in \{\mathbf{x} | Im(\mathbf{x}) = 0\}, \quad (2)$$

where T_0 denotes the time of image acquisition with respect to the emergence of the tumor. This equation basically states that $\tilde{u}$ approximates the actual tumor distribution u at a time instant T_0, in the regions where the image is not showing any tumor. The construction of $\tilde{u}$ starts from the tumor delineation in the image, which is assumed to correspond to an iso-density surface of $u = u_0$, and approximates the u values outside the enhanced area in the image. Unlike the reaction-diffusion models, which are dynamic and describe time evolution of gliomas, the construction of this approximation is a static problem. The only time related parameter in Equation 2 is T_0 and it indicates the time elapsed between the emergence of the tumor and the image acquisition. In clinical situations this value is not available. Therefore, the approximation $\tilde{u}$ cannot depend on T_0.

In the following sections we derive a formulation for constructing the approximation $\tilde{u}$. This formulation is derived from the reaction-diffusion models as given in, [8,18,40]. The building block of these models is the Fisher-Kolmogorov (F-KPP) equation, which is explained in the following section along with the previously proposed related reaction-diffusion models.

2.1 Reaction-Diffusion Models

The form of reaction-diffusion model considered in this work is formulated as:

$$\frac{\partial u}{\partial t} = \nabla \cdot (D(\mathbf{x})\nabla u) + \rho u(1-u) \tag{3}$$

$$D\nabla u \cdot \mathbf{n}_{\partial\Omega} = 0 \tag{4}$$

where u is the normalized tumor cell density between $[0, 1]$ (normalized cell densities will be used throughout this article). The first term on the right hand side, the diffusion term $\nabla.(D(\mathbf{x})\nabla u)$, represents the invasion of the surrounding tissue by tumor cells. The second term, $\rho u(1-u)$, is the reaction term, and it represents proliferation of tumor cells. We note that other types of reaction terms also have been used in the literature both for modeling tumor growth and for other applications [15,47]. Equation 4 corresponds to the Neumann boundary condition, where Ω is the brain, $\partial\Omega$ its boundary (ventricles and the skull) and $\mathbf{n}_{\partial\Omega}$ is the normal to this boundary. It describes the fact that tumor cells do not diffuse through ventricles nor through the skull.

Different models using Equation 3 vary in the way they construct the *tumor diffusion tensor* D and in their reaction term. In this work we focus on the models which take into account the differential motility of tumor cells as observed by Giese *et al.* in [14]. The first such model was proposed by Swanson *et al.* in [39], where the tumor cells are modeled to diffuse isotropically with tissue dependent rates. Building on this work, following the observation that tumor cells follow the white matter fiber structures in the brain, Clatz *et al.* in [8] and Jbabdi *et al.* in [18] proposed to model the migration of tumor cells with anisotropic diffusion. In this formulation, D, is derived from the diffusion tensor of water molecules in the brain, D_{water}, (available through DT-MRI) as follows :

$$D(\mathbf{x}) = \begin{cases} d_g I & , \mathbf{x} \in \text{gray matter} \\ d_w D_{water} & , \mathbf{x} \in \text{white matter} \end{cases} \tag{5}$$

where tumor cells are assumed to diffuse isotropically in the gray matter with a rate d_g and diffuse along the white matter tracts proportional to the diffusion tensor of water molecules D_{water}. d_w is the diffusion rate linking D_{water} to tumor diffusion in the white matter. D_{water} in this construction is obtained from DT-MRI and it is normalized such that the highest diffusion rate in the brain would be 1. In this work, we base our methods on these anisotropic reaction-diffusion models.

According to the reaction-diffusion models the tumor cell density distribution beyond the visible part of the tumor depends highly on the 3 parameters d_g, d_w and ρ (later in Section 2.3 we will see that the formulation proposed in this article for extrapolating this distribution actually depends on two parameters d_w/ρ and d_g/ρ). Here, we do not consider the problem of estimating any of these parameters. We assume that these parameters can either be estimated using time series of images [23] or manually changed/adjusted by the user.

The first idea that comes to mind for extrapolating the invisible tumor infiltration is to use the reaction-diffusion equation either in its dynamic form or in its steady-state form (assuming $u_t = 0 = \nabla \cdot (D\nabla u) + \rho u(1-u)$). Unfortunately, this idea cannot be applied directly. Solving the steady-state form of the equation provides us the static cell density distribution (u=1 for the reaction-diffusion equation used here) which is constant over time. When we consider the unstable nature of brain gliomas and tumors in general, this solution seems unreasonable for the task. The dynamic form of the equation on the other hand, solves a temporal evolution. This means starting from an initial condition (initial distribution of tumor cell densities) and evolving it to obtain the cell distributions at later times. When we consider the problem of extrapolating the cell densities in a single image, using the dynamic form requires:

- estimating/assuming an initial condition of the cell density distribution of the tumor at an earlier instant than the image acquisition and
- running the temporal evolution starting from this initial condition for some amount of time such that the image created by this simulated distribution matches the actual observed image.

This strategy bears two issues. The first is that the initial condition should be guessed if we do not have a previously available image. Even if such an image is available we still have to solve the problem of extrapolating infiltration extent in that image. The second problem is that even if we somehow assume the initial tumor distribution, we are not sure that the result of the simulation will match the exact tumor delineation we observe in the image. The proposed method in this work overcomes these problems by using only the tumor delineation visible in the image without assuming previous tumor cell distributions.

2.2 Asymptotic Properties of the F-KPP equation

The F-KPP equation has some desirable properties which enable us to derive the extrapolation formulation. The 1D version of this equation with constant coefficients and no boundary conditions was first proposed by Fisher [12] to model the spread of a favored gene in a population. The possible solutions of this 1D equation have been studied thoroughly by Kolmogorov. Later on Aronson et al. extended this analysis to higher dimensions in [2]. Here we wish to summarize some relevant results in these works for the case of infinite cylinder in 3D.

In the constant coefficient case Equation 3 admits a traveling wave (a planar wave) solution in the infinite cylinder (the change of u is non-zero in only one

direction). Letting $\mathbf{n}$ denote the direction of the infinite cylinder, the traveling wave solution can be written as:

$$u(\mathbf{x},t) = u(\mathbf{n}\cdot\mathbf{x} - ct) = u(\overline{\xi}) \quad \text{as} \quad t \to \infty \tag{6}$$

where c is the speed of the front and $\overline{\xi} = (\mathbf{x}\cdot\mathbf{n} - ct)$ is the moving frame of the traveling wave. As a result of the nonlinear reaction term the origin of the moving frame $\overline{\xi} = 0$ is set at $u = 0.5$ [2,46]. The most interesting property of the F-KPP equation for us is that when Equation 3 is initialized with an initial distribution $u(\mathbf{x}, t = 0)$ (with compact support in the infinite cylinder) $u(\mathbf{x}, t)$ takes the form of a traveling wave for large times. Figure 2 illustrates the convergence of the shape of u both for the whole front (a) and for the low density parts (b).

In order to solve for this traveling wave solution we plug $u(\overline{\xi})$ into the reaction-diffusion equation and obtain the constant coefficient non-linear ordinary differential equation (ODE)

$$\mathbf{n}^T D\mathbf{n}\frac{d^2u}{d\overline{\xi}^2} + c\frac{du}{d\overline{\xi}} + \rho u(1-u) = 0. \tag{7}$$

In order for this equation to have admissible solutions, the speed of the front c should be a constant. This constant depends on the diffusion tensor D and ρ. Different initial u distributions converge to different traveling waves and these waves have different c values. However, in the case the initial condition has a compact support, c can be given as, [2]:

$$c = 2\sqrt{\rho\mathbf{n}^T D\mathbf{n}} \tag{8}$$

The solution of the nonlinear ODE given in Equations 7 and 8 is the traveling wave solution. It does not have a simple analytical form due to the nonlinear reaction term. In the next section we propose a way to solve this equation and construct the infiltration extent.

We would like to note here that the traveling wave characteristics of reaction-diffusion models in the context of tumor growth modeling was also used by Swanson *et al.* in [42]. Although they did not use them specifically for extrapolating the tumor distribution, the authors used these characteristics to estimate approximate parameters of the model. However, their methods do not work directly with the visible tumor. They find the sphere with the same volume as the visible tumor and use that in computations. This approach does not take into account the differential motility of tumor cells, tissue inhomogeneity and the fiber structure available in the patient images. In order to extrapolate the infiltration margins realistically, we propose a method that takes these patient-specific information into account using the images.

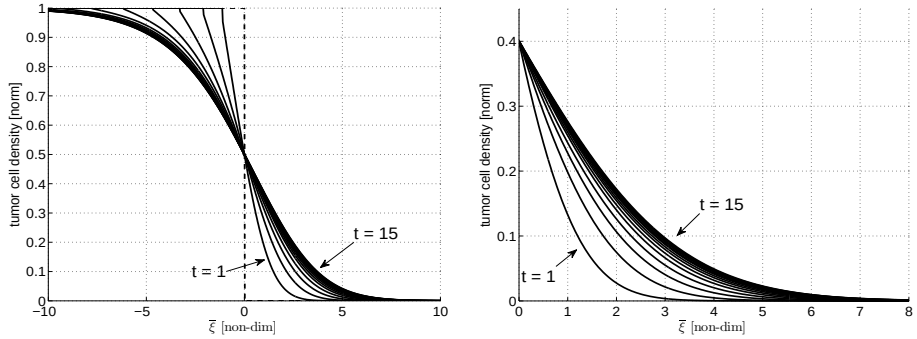

(a) (b)

Fig. 2. (a) The tumor distribution evolving with the constant coefficient reaction-diffusion equation (cross-section of the tumor cell density distribution in the infinite cylinder) is plotted at different times (non-dimensional). We plot the distribution at different times on the moving frame $\overline{\xi}$. Observe that as time passes the shape of the distribution converges to an asymptotic shape. (b) When we plot the distribution below $u = u_0$ we again observe the convergence.

2.3 Low Density Profile Extrapolation

The asymptotic properties of F-KPP equations explained in the previous section help us construct the extrapolation method we seek for. We use the asymptotic solution given in Equation 6 as the approximation for the tumor cell density distribution beyond the visible part of the tumor in the image, namely the $\tilde{u}$. Note that this solution is independent of time. However, before we can use it there are two problems to be solved. The first one is that we do not have an analytical form of the solution. The second problem is that the asymptotic solution exists in the infinite cylinder in the case of constant coefficients. So we have to generalize this to more general curved solutions under spatially varying coefficients.

As we note in the previous section, Equation 7 does not have an easy-to-find analytical solution. The reason is the nonlinear reaction term. Since we cannot find the exact solution we approximate it. The initial idea is to linearize the nonlinear term around $u = 0$ [22]. This gives us a linear ODE whose solution can be found analytically, which in return can be used as an approximation for the solution of the nonlinear ODE. However, this attempt assumes that $u(1-u)$ can be well approximated by u. This is only true for very low values of u ($u < 0.1$). So instead of this global linearization, in this work, we propose to use local linearization. The main idea is to locally linearize the nonlinear term around a point $u(\overline{\xi^*}) = u^*$, find the analytical solution of the resulting linear ODE for the small neighborhood around u^* and then combine the solutions on different neighborhoods to obtain the global approximation. One way to

linearize Equation 7 around the point $(\overline{\xi}^*, u^*)$ is

$$D_{\mathbf{n}} \frac{d^2u}{d\overline{\xi}^2} + 2\sqrt{\rho D_{\mathbf{n}}} \frac{du}{d\overline{\xi}} + \rho u(1-u^*) = 0, \quad D_{\mathbf{n}} = \mathbf{n}^T D \mathbf{n}. \tag{9}$$

This gives us a linear ODE whose solution can be found analytically. After some derivations (see Appendix A for the details on this derivation) the solution of this equation $\tilde{u}_{\overline{\xi}^*}$ can be given as

$$\tilde{u}_{\overline{\xi}^*} = u^* e^{-\lambda(1-\sqrt{u^*})\xi}, \quad \lambda = \sqrt{\rho / D_{\mathbf{n}}}. \tag{10}$$

We notice that the variable used in this solution is not $\overline{\xi}$ but ξ. The difference is that ξ is a shifted version of the moving frame $\overline{\xi}$ and its origin $\xi = 0$ is at the point $u = u^*$. Therefore, ξ denotes the distance from this point. Such solutions can be constructed for different neighborhoods covering the whole line of values of $u \in [0, 1]$. Naturally for each of these local patches the linear approximation gets better as we go closer to the center of the neighborhood towards u^*. We can go further and reduce the size of each neighborhood, increasing the number of neighborhoods needed to cover all possible values of u. Combining infinitesimally small neighborhoods and using the fact that we know the location of the point $u = u_0$, we can write the global approximation for the solution of the nonlinear ODE, in other words, for the form of the traveling wave as

$$\tilde{u}(\mathbf{x}) = \int_0^x -\lambda(1-\sqrt{\tilde{u}})\tilde{u} d\xi, \quad \tilde{u}(0) = u_0, \quad \lambda = \frac{\sqrt{\rho}}{\sqrt{\mathbf{n}^T D \mathbf{n}}}. \tag{11}$$

where x is the distance of the point $\mathbf{x}$ from the known point $u = u_0$ (see Appendix A for details). We recall that in our context $\mathbf{x}$ is the distance from the tumor delineation. The solution $\tilde{u}$ as given in Equation 11 enables us to extrapolate values of u beyond the point $u = u_0$.

We would like to diverge from the topic for a moment and give insight on the nature of $\tilde{u}$. The expression given in Equation 11 is an approximation to the solution of the ODE given in Equation 7 which corresponds to the Fisher-Kolmogorov equation (given in 3). Since it is an approximation, it does not solve the equation. Let us define

$$L(u) = \mathbf{n}^T D \mathbf{n} \frac{d^2u}{d\overline{\xi}^2} + 2\sqrt{\rho \mathbf{n}^T D \mathbf{n}} \frac{du}{d\overline{\xi}} + \rho u(1-u) = 0. \tag{12}$$

Now, $\tilde{u}$ is not necessarily a solution of L since we constructed it as an approximation to the solution of L. Therefore we expect

$$L(\tilde{u}) = R(\tilde{u}) \neq 0, \tag{13}$$

where R is the residual term. When we place $\tilde{u}$ in L and solve for R using the fundamental theorem of calculus we find it to be $R(\tilde{u}) = (\rho/2)\tilde{u}[\tilde{u} - \sqrt{\tilde{u}}]$. When we add this term to the Equation 7, we obtain the equation:

$$\tilde{L}(u) = L(u) + R(u) = \mathbf{n}^T D\mathbf{n}\frac{d^2u}{d\overline{\xi}^2} + c\frac{du}{d\overline{\xi}} + \rho u(1 + \frac{\sqrt{u}}{2} - \frac{3}{2}u) = 0, \qquad (14)$$

in which $\tilde{L}(\tilde{u}) = 0$. This gives us another view of the local linearization presented above. We see that approximating u with $\tilde{u}$ can also be seen as approximating L with $\tilde{L}$ or approximating the nonlinear term $\rho u(1-u)$ with $\rho u(1 + \frac{\sqrt{u}}{2} - \frac{3}{2}u)$.

In order to compare $\tilde{u}(\mathbf{x})$ with $u(\mathbf{x}, t)$, in a coherent manner with our medical context, we simulate the growth of a virtual tumor in the infinite cylinder with constant (non-dimensional) coefficients using the model given by Equations 3 and 4 (see [27] for details on non-dimensionalization). The cell density distribution u of this tumor is known for all the points in the domain however, not visible in its images. We assume that the detection of the tumor takes place when its visible part has grown up to 1.5 cm in diameter. We create a synthetic image by setting the detection threshold to $u_0 = 0.4$. We then take 8 more images of the same tumor each 1 time unit (non-dimensional time) apart. For each of these 9 images we reconstruct the tumor cell density distribution beyond the point $u = 0.4$ using Equation 11. Then we compare $\tilde{u}$ with the actual tumor distribution u. In Figure 3 we plot the approximation $\tilde{u}$ (solid curve) together with the part of the actual distribution u not visible in the images (dashed curves). We show the form of the u at the time of different image acquisitions. We observe that the quality of $\tilde{u}$ in approximating u depends on the time the image is taken. When the image is taken in a latter time then $\tilde{u}$ provides a better approximation for the tumor cell density distribution u. The table accompanying Figure 3 shows the difference between the actual distribution u and the approximation $\tilde{u}$ in the different images. We see that although this difference depends on time, it remains reasonably low for all the images showing that $\tilde{u}$ would serve as a good approximation regardless of the time the image was taken. We also observe that the discrepancy between the actual distribution and the approximation first decreases, then increases after image 5 and converges later on. This is due to $\tilde{u}$ being an approximation of the traveling wave solution. Therefore, as the tumor profile converges to the traveling wave solution the discrepancy between $\tilde{u}$ and the profile converges to the difference between $\tilde{u}$ and the traveling wave.

The approximation given in Equation 11 is derived for the case where the coefficients of the F-KPP equation are constant over the whole domain and the motion is only in one direction, which is not the case for general media and hence, for the brain. Moreover, when the tumor front is curved, its motion would not be in one direction and the solution of the F-KPP equation

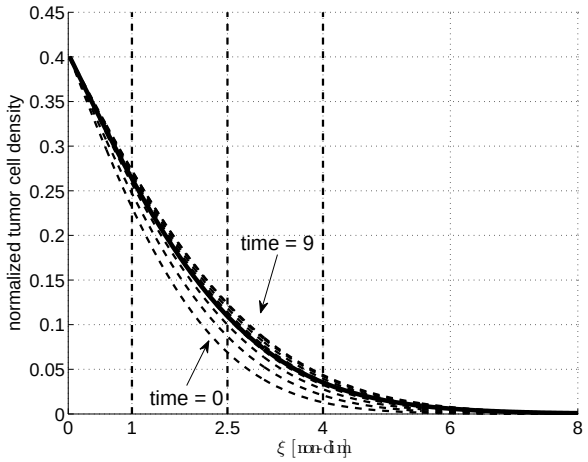

image	density difference at 1.0	at 2.5	at 4
1	0.037	0.044	0.024
2	0.021	0.026	0.016
3	0.010	0.013	0.010
4	0.005	0.005	0.005
5	1×10^{-4}	-0.001	-0.001
6	-0.003	-0.005	-0.002
7	-0.006	-0.008	-0.006
8	-0.006	-0.009	-0.006
9	-0.006	-0.009	-0.006

Fig. 3. The tail approximation $\tilde{u}$ constructed using Equation 11 (solid curve) is plotted with the actual tails of the tumor front u. All the time and distance values are dimensionless. To give an idea, for a high grade glioma each time unit would correspond to 60 days and each distance unit would correspond to 0.5 cm. The associated table shows the difference in tumor cell density between the tail approximation and the actual tail at a given image for different locations in the moving frame denoted by the vertical dashed lines in the figure.

cannot be given in terms of a traveling wave. In order to apply Equation 11 in the general setting we make the following assumptions: within a voxel, the coefficients are constant and the motion of the front is only in one direction. Based on these assumptions we can construct the local approximation given in Equation 11 in each voxel separately. The computation in each voxel uses the values at its neighbors as it is the case for the reconstruction in the infinite cylinder. Using this principle, we sweep the domain starting from the visible part of the tumor and going outwards computing the tumor cell density esti-

mate at each voxel. In this construction the direction of motion and the initial value for each voxel are defined by its adjacent voxels.

Following our assumptions, the integrand in Equation 11 can be written as the gradient relation in 3D,

$$\frac{\partial \tilde{u}}{\partial \mathbf{n}} = \lambda(1 - \sqrt{\tilde{u}})\tilde{u}. \tag{15}$$

Placing λ in this equation and replacing $\mathbf{n}$ with $\nabla\tilde{u}/ \mid \nabla\tilde{u} \mid$, we obtain the following static Hamilton-Jacobi equation that constructs the approximation $\tilde{u}$ given in Equation 2 at each voxel.

$$\frac{\sqrt{\nabla\tilde{u} \cdot (D\nabla\tilde{u})}}{\sqrt{\rho}\tilde{u}(1 - \sqrt{\tilde{u}})} = 1,\ \tilde{u}(\Gamma) = u_0 \tag{16}$$

where Γ is the contour around the visible part of the tumor in the image ($u >= u_0$). Notice that the information that the boundaries of the tumor delineation corresponds to the iso-density contour $u = u_0$ is embedded as a Dirichlet type boundary condition. We also remind that the fiber structure available through DT-MRI and the tissue inhomogeneity are embedded in the spatially varying D tensor.

Equation 16 has two solutions at each point, one with increasing and the other one with decreasing $\tilde{u}$. Since the reaction-diffusion equation tells us that as we move away from the visible contour, the values of $\tilde{u}$ will decrease therefore, for all points we choose the decreasing solution. Using Equation 16 we can start from Γ and sweep the domain moving outwards as we find $\tilde{u}$ values for each voxel.

The Equation 16 is a static Hamilton-Jacobi equation. Several different numerical methods have been proposed to solve this kind of equations [30,34]. In this work, we adopt a fast marching (FM) based approach to solve it which is coherent with the sweeping idea we propose to construct the low density infiltration estimate $\tilde{u}$. The original FM method as proposed by Sethian and Osher solves the Eikonal equation but does not take into account the anisotropy [33]. The method we use, detailed in [24], modifies the original FM algorithm to include the effect of the anisotropy. In this way it enjoys the efficiency of the FM method and provides an accurate solution in the case of high anisotropy. As a result of sweeping the domain outwards and using the mentioned numerical scheme to solve the Equation 16, the continuity of the constructed $\tilde{u}$ is ensured. The implicit interpolation between different voxels, in other words the patching between planar solutions in different voxels, depends on the order of the numerical scheme, which is linear in our case.

The estimate for low density infiltration of gliomas as constructed by Equation 16 is derived based on Equation 3. It does not take into account effects of the Neumann boundary condition given in Equation 4. This condition states that tumor cells trying to pass across the boundary (skull and ventricles) bounce back from it and continue their motion within the tissue. When we consider the Brownian motion interpretation of the diffusion process, this bouncing back mechanism is the large scale abstraction of tumor cells continuing their random motion towards the brain when they encounter the boundary. Therefore, the effects of the Neumann boundary condition are not only confined to the points neighboring the boundary. The condition affects the tumor cell density distribution throughout the brain.

We use the *method of reflection* (method of images) to include the effects of the Neumann boundary conditions in our extrapolation method [38]. Method of reflection constructs solutions of linear partial differential equations such as the diffusion equation in finite domains. Here, we use the same approach for the nonlinear Equation 3. In order to use the same method for nonlinear equations we make some assumptions about the nonlinearity which are detailed in Appendix B. In order to satisfy the boundary condition given in Equation 4, we use superposition of two different approximations each in the form of Equation 16

$$\tilde{u} = \tilde{u}_{nb} + \tilde{u}_{ref}, \tag{17}$$

where $\tilde{u}$ is the final approximation. The first approximation $\tilde{u}_{nb}$ is the same as the one given in Equation 16 with a different Dirichlet boundary condition. It ignores boundaries and constructs the approximation starting from the tumor delineation Γ:

$$\frac{\sqrt{\nabla \tilde{u}_{nb} \cdot (D \nabla \tilde{u}_{nb})}}{\sqrt{\rho} \tilde{u}_{nb}(1 - \sqrt{\tilde{u}_{nb}})} = 1, \quad \tilde{u}_{nb}(\Gamma) = \mathbf{u_{nb}}(\Gamma). \tag{18}$$

Notice that instead of setting the value of $\tilde{u}_{nb}(\Gamma)$ to u_0 we set it to a function $\mathbf{u_{nb}}(\Gamma)$. The reason for this difference in the Dirichlet boundary condition is that we use the superposition of two approximations instead of using only $\tilde{u}_{nb}$. This difference will become clear shortly. For now, let us assume this function is known. In our scheme we first construct $\tilde{u}_{nb}$ and based on it we construct the second approximation $\tilde{u}_{ref}$ by

$$\frac{\sqrt{\nabla \tilde{u}_{ref} \cdot (D \nabla \tilde{u}_{ref})}}{\sqrt{\rho} \tilde{u}_{ref}(1 - \sqrt{\tilde{u}_{ref}})} = 1, \quad \tilde{u}_{ref}(\partial\Omega) = \mathbf{u_{ref}}(\partial\Omega). \tag{19}$$

The aim of $\tilde{u}_{ref}$ is to include the effect of the boundary condition on the tumor

cell density distribution inside the brain. We see that the construction of $\tilde{u}_{ref}$ is initialized on the boundary $\partial\Omega$ as opposed to the construction of $\tilde{u}_{nb}$. This corresponds to the bouncing mechanism and $\tilde{u}_{ref}$ is the tumor distribution bouncing back from the boundary. We define the Dirichlet boundary condition $\tilde{u}_{ref} = \mathbf{u_{ref}}$ such that $\tilde{u}$ satisfies the Neumann boundary condition of the reaction-diffusion model, $D\nabla\tilde{u} \cdot \mathbf{n}_{\partial\Omega} = 0$. Imposing this condition defines

$$\mathbf{u_{ref}}(\mathbf{x}) = -\frac{\mathbf{n}_{\partial\Omega}^T D\mathbf{n}}{\sqrt{\mathbf{n}^T D\mathbf{n}}\sqrt{\mathbf{n}_{\partial\Omega}^T D\mathbf{n}_{\partial\Omega}}}\tilde{u}_{nb}(\mathbf{x}), \quad \text{for } \mathbf{x} \in \partial\Omega, \tag{20}$$

where $\mathbf{n}_{\partial\Omega}$ is the normal direction on the boundary point $\mathbf{x}$ and $\mathbf{n}$ is the gradient direction of $\tilde{u}_{nb}$. The derivation of this criteria is given in details in Appendix C. Once $\mathbf{u_{ref}}$ is defined we can construct $\tilde{u}_{ref}$. Now, coming back to the question of defining $\mathbf{u_{nb}}$ in Equation 18, we use the modeling assumption $u(\Gamma) = \tilde{u}(\Gamma) = u_0$, which states that the boundaries of the tumor delineation in the image corresponds to an iso-density contour of the tumor cell density distribution. The relation

$$\tilde{u}(\mathbf{x}) = \tilde{u}_{nb}(\mathbf{x}) + \tilde{u}_{ref}(\mathbf{x}) = \mathbf{u_{nb}}(\mathbf{x}) + \tilde{u}_{ref}(\mathbf{x}) = u_0, \quad \text{for } \mathbf{x} \in \Gamma \tag{21}$$

gives us the function $\mathbf{u_{nb}}$. In this construction we notice that $\tilde{u}_{ref}$ and $\tilde{u}_{nb}$ depends on each other and we have two conditions that defines them. We use an iterative algorithm to solve for $\tilde{u}_{ref}$ and $\tilde{u}_{nb}$. This algorithm is given in Algorithm 1. It summarizes the proposed scheme for constructing the approximation $\tilde{u}$ in the presence of the Neumann boundary condition.

Algorithm 1 The iterative algorithm for extrapolating the tumor cell density distribution beyond the tumor delineation in the image. The resulting $\tilde{u}$ takes into account the Neumann boundary conditions.

Initialize the extrapolation: $\mathbf{u_{nb}}^0 = u_0$
repeat
  construct $\tilde{u}_{nb}^i$ based on the method explained in Section 2.3 starting from Γ, the tumor delineation.
  set $\mathbf{u_{ref}}^i$ using Equation 20 for $i \geq 1$
  construct $\tilde{u}_{ref}^i$ (the method in Section 2.3) starting from $\partial\Omega$, the brain boundaries.
  $\mathbf{u_{nb}}^{i+1} = u_0 - \tilde{u}_{ref}^i|_\Gamma$ for $i \geq 1$
until Equations 20 and the Neumann condition are satisfied with enough accuracy.
set $\tilde{u} = \tilde{u}_{nb} + \tilde{u}_{ref}$

In Figure 4, for a simple 2-D example, we show the low density infiltration regions computed by solving the reaction-diffusion equation (a) and the extrapolated approximation $\tilde{u}$ taking into account the Neumann boundary conditions (d). In the image, we also plot the two parts of the superposition $\tilde{u}_{nb}$ and $\tilde{u}_{ref}$

in (b) and (c) respectively. Comparing the contour plots (a) and (d) we observe that the effect of the Neumann boundary condition is well captured by adapting the method of reflection in the low density infiltration extrapolation even for complex boundaries.

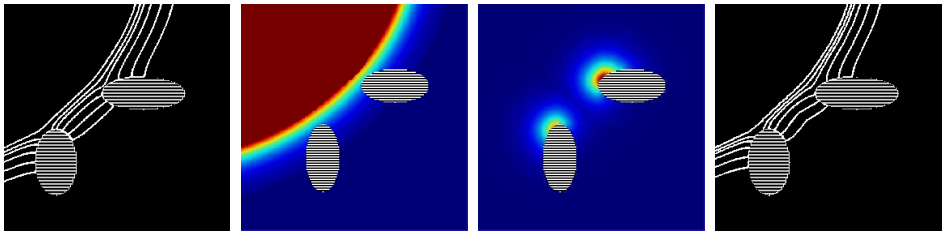

(a) (b) (c) (d)

Fig. 4. The 2-D example shown in the figures, demonstrates the two parts of the estimation $\tilde{u}$ and the effect of including the boundary reflection. The striped regions are set to be the boundaries with the Neumann boundary condition. (a)The result of the reaction-diffusion equation for the low density region $0.002 \leq u \leq 0.08$ shows the actual iso-density contours. (b) The no boundary part of the low density region extrapolation $\tilde{u}_{nb}$, (c) The reflection part $\tilde{u}_{ref}$, (d) The iso-density contours of the superposition: Low density region estimation $\tilde{u}$.

3 Results and Experiments

In Section 2 we presented a method for extrapolating the low density infiltration of gliomas $\tilde{u}$ in MR images. This method offers a solution to the problem of limited tumor density visualization of medical images.

In this section, we assess the quality of the extrapolation method and the constructed estimation $\tilde{u}$, using synthetic tumors simulated by the reaction-diffusion growth model. First we compare the actual tumor cell density distribution beyond the visible mass with the estimation $\tilde{u}$ constructed by the proposed method. In the second part we propose a method to tailor irradiation margins based on the estimated low density infiltration. We then compare this tailored irradiation margin with the conventionally used constant one through geometric comparisons. These comparisons include the number of tumor cells **not** targeted and the volume of healthy tissue set to be irradiated.

Both of the mentioned experiments are done on MR images, where we use a data set taken from a healthy subject. This dataset consists of T1 weighted, T2 weighted and diffusion tensor images (DTI) with the resolution of $1mm \times 1mm \times 2.6mm$. We simulate the growth of 8 different synthetic tumors in two different locations using the reaction-diffusion model explained in Section 2.1. We initialize 4 in the frontal lobe and 4 in the parietal lobe as shown in Figure 5(a) and (b). We choose these two locations with different tissue

compositions to test the effect of tissue heterogeneity in our experiments. The difference between the tumors at the same location is obtained by using different growth parameters (diffusion coefficients and proliferation rates). We use 4 different parameter sets as given in the table accompanying Figure 5. Each tumor was initialized in a single voxel and grown in the MR image. In order to create the synthetic images of these tumors, the simple imaging process given in Equation 1 is applied to each tumor. We recall that this process marks a voxel as tumoral if the number of tumor cells exceed u_0. In our case we take $u_0 = 0.4$ meaning 40% of the maximum tumor cell capacity the brain parenchyma can handle (this value is consistent with the value proposed in [45]). For each tumor, the detection and the first image acquisition take place when the visible tumor reaches the size of 1.5 cm in diameter. After the detection a synthetic image is created every 50 days using the image function Im given in Equation 1. These images are then used as the inputs to our extrapolation method to estimate their low density infiltration distributions. We perform our comparisons for each of these images independently.

The computation time to run the extrapolation method in the synthetic images depends on different factors such as u_0, D, ρ, the tumor location or the desired accuracy of the iterative method for including boundary conditions. As an example, in our simulations it took around 5 minutes to extrapolate the low density distribution of the tumor at the frontal lobe with high diffusion rate, starting from $u_0 = 0.4$ to $u = 1\times10^{-5}$ using a 4Gb memory 2.26GHz computer.

3.1 Assessing the Estimation Quality

In order to quantitatively compare the *spatial resemblance* of the extrapolated cell density distribution with the actual one, we compute the distance between the corresponding iso-density contours (an example is shown in Figure 6). We define the measure of spatial resemblance as follows. For the density value v in the image taken at time t we define the error measure $\epsilon_v(t)$.

$$\begin{aligned} \epsilon_v(t) &= \frac{1}{2}[dist(\Gamma_1^v, \Gamma_2^v) + dist(\Gamma_2^v, \Gamma_1^v)] \\ \Gamma_1^v &= \{x | u(x,t) = v\} \\ \Gamma_2^v &= \{x | \tilde{u}(x,t) = v\} \\ dist(A,B) &= \frac{1}{\sharp A}\sum_{a\in A} dist_{min}(a,B), \end{aligned} \tag{22}$$

where $dist_{min}(a, B)$ is the minimum Euclidean distance between point a and the set B, v is a density value for which the iso-density surfaces of u and $\tilde{u}$ are extracted. Using this, the total resemblance measure between the two

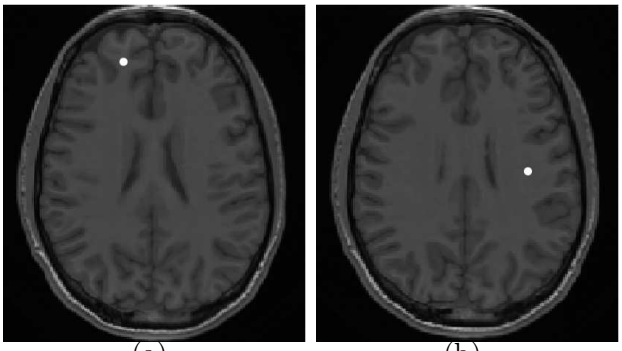

(a) (b)

name	$d_w[mm^2/day]$	$d_g[mm^2/day]$	$\rho[1/day]$
high $d_{w,g}/\rho$	0.5	0.025	0.009
low $d_{w,g}/\rho$	0.25	0.01	0.012
lower anisotropy	0.25	0.15	0.012
higher anisotropy	0.5	0.005	0.012

Fig. 5. Figures (a),(b): Different tumor seeds used in the experiments are shown. Table: Different diffusion and proliferation rates used for the simulations. 8 different tumors are created with this 4 set of parameters in the locations given in Figures (a) and (b). The different parameters are chosen such that the evolution of the visible tumor's size (in volume) would be similar for all the tumors.

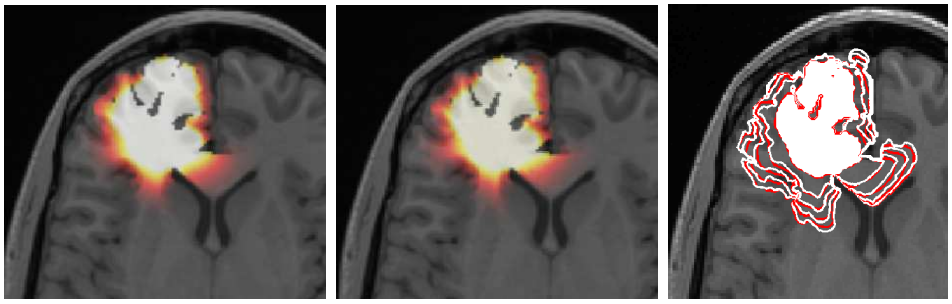

(a) Actual Profile (b) Extrapolated Tails (c) Comparison

Fig. 6. Example of an extrapolated image for a synthetic tumor. (a) The image of a synthetic tumor is shown, where the white region is the visible part. The not-imageable infiltration region is also shown in color (from yellow=high density to red=low density). (b) The low density infiltration extrapolated by the proposed method starting from the visible part. (c) Iso-density contours of the actual distribution (red solid) and the corresponding ones of the extrapolated distribution (white solid). We observe the high global resemblance.

distributions for an image taken at time t is defined as:

$$\epsilon(t) = \frac{1}{\mathcal{V}} \sum_{v \in V} \epsilon_v(t) \tag{23}$$

where V is the set of density values spanning the low density region. We have 16 iso-density values in the set V with the minimum $v_{min} = 0.005$. Different values are logarithmically spaced to ensure that the corresponding iso-density contours will be equally spaced (due to the exponential drop of the front profile). The global error criterion $\epsilon(t)$ is the average over different density values and provides a spatial resemblance measure.

In Figures 7(a) and (b) we plot $\epsilon(t)$ for different time instances (images) showing the resemblance between the estimated and the actual tumor cell density distributions. We also plot the error measure for tumors with different diffusion and proliferation rates and for tumors at different locations (one at a region with heterogeneous tissue type and the other at a region with homogeneous tissue type). In Figure 7(c) and (d) we plot v vs. $\epsilon_v(t)$ for the image taken at day 200 after the detection. These plots show the change of the error measure with respect to the iso-density contour value.

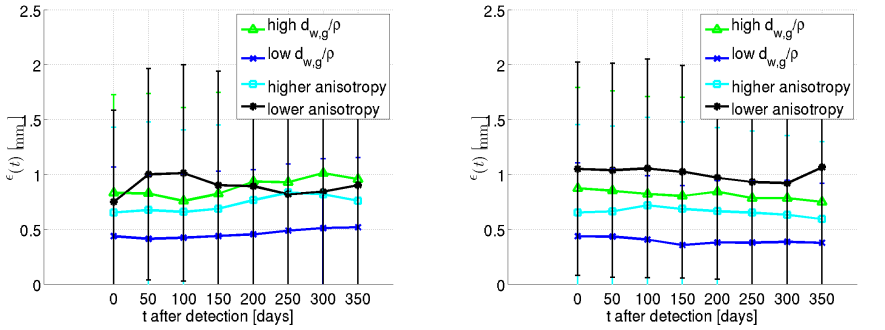

(a) Homogeneous tissue region (b) Heterogeneous tissue region

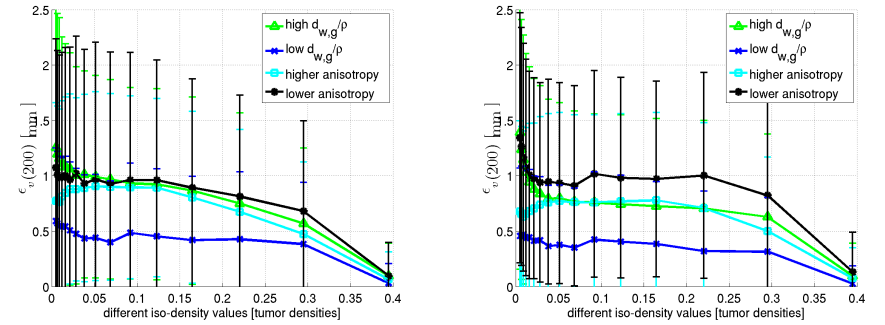

(c) Homogeneous tissue region (d) Heterogeneous tissue region

Fig. 7. (a),(b) The average extrapolation error as a function of image acquisition time, $\epsilon(t)$ (Equation 23). (c),(d) The extrapolation error as a function of the density value of the extrapolated contour, for the image taken at day 200, $\epsilon_v(200)$ (Equation 22). In both cases, the average approximation error $\epsilon(t)$ remains within a few voxel, smaller than 1.07 mm in all cases.

Observing Figures 7 we notice that the mean and the first standard deviation of the difference between the two profiles remain within the range of

$(0, 2.5)mm$. This shows that the extrapolated distribution remains within 1 to 2 voxel distance from the actual one (voxel size is $1 \times 1 \times 2.6\ mm^3$). This similarity demonstrates the quality of the proposed approximation in two ways: (1) The resemblance in the shape of the cell distribution, which tells us that the proposed method captures the differential motility of tumor cells the way it is described in reaction-diffusion models. (2) The corresponding iso-contours of the two distributions are at the same distance from the tumor delineation. This empirically proves that the asymptotic solution of the reaction-diffusion equation, the traveling wave, is a good approximation of the cell distribution for clinically relevant time ranges. Analyzing the change of $\epsilon(t)$ and $\epsilon_v(200)$ with respect to several parameters, we can state the followings about the quality of the extrapolation method in approximating the low density parts of a reaction-diffusion tumor:

- The average distance between the two distributions is around 1.0 mm (less than 1.07 mm) for all cases. The worst case error is reached at day 350 for the tumor in the parietal lobe and at day 100 for the tumor in the frontal lobe. However, the change of the mean error in time is not significant.
- *When the ratio between the diffusion rate and the proliferation rate (d/ρ) is low, the discrepancy between the extrapolated distribution and the real one is lower.* When this ratio is high the error seems to be higher. Examining the difference between Equations 7 and 14 we expect the approximation error to increase when we increase ρ, contrary to the observation. The reason for the observed decrease in the error is the influence of the size of the infiltration extent. Low d/ρ ratio indicates lower dispersion rate of tumor cells which yields smaller infiltration extent. Extrapolating a smaller space brings lower error because we accumulate less error in the construction of the approximation. The extrapolation method starts from the tumor delineation and sweeps the domain outwards. This outwards sweeping accumulates errors as we go further away from the tumor delineation. This factor becomes dominant and explains the observed behavior. Moreover, we estimate the tumor cell distribution created by a reaction-diffusion process with a convection one. As the process is dominated by diffusion the effect of the curvature on the profile increases and raises the discrepancy.
- *When the anisotropy coefficient d_w/d_g is higher the extrapolation is almost all the time closer to the actual distribution.* (Except at day 250 for the tumor in the homogeneous tissue the two errors seem to be the same.) The reason is the increased grey matter diffusion. As we note in the previous item, we introduce an error when we use convection to approximate diffusion. As the diffusion rate in the grey matter increases the approximation error also increases resulting in a higher discrepancy between the extrapolated and the actual distribution. When the diffusion is more isotropic we introduce the approximation error all over the tumor surface increasing the mean error.
- *$\epsilon_v(t)$ increases as v decreases suggesting that the difference between the ex-*

trapolated and the actual distribution increases as we move away from the visible part of the tumor. This is due to our construction of the extrapolation as an integral solution which causes an accumulation of errors. However, the mean error in this case remains below 1.5 mm for all cases, which corresponds to 1.5 voxels in the acquisition plane.

- Although we see some difference between the $\epsilon(t)$ and $\epsilon_v(t)$ plots for the tumors placed in different locations of the brain, it is not significant to draw a conclusion about the effect of the tissue composition on our formulation.
- Observing Figures 7 (a) and (b) we see that the approximation error remains almost constant as time increases. Considering that the proposed method uses the asymptotic solutions of reaction-diffusion equations we expect the error to decrease as time increases. However, increasing time has two effects on the approximation error. The first effect is the expected decrease as explained above. However, there is a second effect with a negative influence on the error. As time increases the extent of the infiltration gets larger. A larger extent means more accumulated error in the construction of the extrapolation. The effects of these two errors cancel each other out yielding a non-decreasing approximation error.

3.2 Comparing Irradiation Margins

Radiotherapy is a spatial (geometry dependent) treatment. The target irradiation region is constructed based on the shape of the tumor visible in medical images. It contains the visible tumor plus a constant margin around the delineation to deal with the low cell density infiltration of the tumor not visible in images. This constant margin approach does not take into account the growth tendencies of the tumor, particularly the differential motility of tumor cells in the white and the gray matters.

The method to extrapolate the low cell density infiltration of gliomas proposed in this work, gives us the opportunity to tailor irradiation regions based on growth dynamics of these tumors as described by the reaction-diffusion models. In order to demonstrate this, in this section we construct *variable* irradiation margins based on the extrapolated densities. We compare the targeting efficacy of such margins with the conventionally used constant margins in the case of synthetic tumors simulated by F-KPP models explained in 2.1. In the construction of the variable margin, we use the same quantity of irradiation as the constant margin (same total volume to be irradiated) but reshape it according to the extrapolated low density infiltration.

Since for the synthetic tumors, the cell density at every location is known, we carry out a quantitative comparison. We do this by testing the *spatial accuracies* of both of these approaches via two different clinically critical measures:

- R: number of tumor cells **not** targeted
- Vol: volume of healthy tissue targeted by the irradiation margin.

Up to now in this article we always used normalized tumor cell densities. In this part, in order to compute the R value we need to return to the dimensional form. Following the values given in [45] we assume that a voxel of $1 \times 1 \times 2.6\ mm^3$ can hold a maximum of 9.1×10^4 tumor cells. Multiplying this value with the non-dimensional tumor density provides us the number of tumor cells. In order to compute the Vol value we need to define "healthy tissue". At the time of detection of high grade gliomas, isolated tumor cells can be found in any region in the brain. Therefore, there is no completely healthy brain tissue. In this work we define a voxel to be healthy if there are on the average less than 1 tumor cell in it. In terms of normalized values the tumor cell density value in a healthy voxel should be less than $1 \times 10^{-5} \approx 1/9.1 \times 10^4$.

We construct the constant margin irradiation region M_c by taking the $2cm$ margin around the visible part of the tumor and removing the skull and the ventricles from it as shown in Figure 8(b). The construction of the variable margin irradiation region M_v is done in two parts. First we extrapolate the infiltration extent of the tumor $\tilde{u}$. We then create M_v^1 by thresholding $\tilde{u}$ at δ whose value will be specified below. M_v^1 holds all the information about the possible infiltration extent of the tumor. However, we know that $\tilde{u}$ has some discrepancy with the hypothetical distribution as shown in Section 3.1. In the second step, we compute a constant error margin around M_v^1, called the M_v^2, which takes into account this discrepancy. The variable irradiation margin M_v is the union of these two regions. In Figure 8(c) we show an example of a variable margin constructed for one of the synthetic tumors. In order to ensure that the amounts of irradiation (assumed to be given by the volume) in M_c and M_v are the same, we tailor the different parts of M_v as

$$\begin{aligned} M_v^1 &= \{x | \tilde{u}(x,t) > \delta\} \\ M_v^2 &= \{x | dist_{M_v^1}(x) < \epsilon_d\} \\ \text{choose } \delta \text{ such that } Vol(M_v^1 \cup M_v^2) &= Vol(M_v) = Vol(M_c). \end{aligned} \tag{24}$$

where $dist_{M_v^1}$ is the distance transform in the brain from the set M_v^1, ϵ_d is the error margin we would like to include in our irradiation region and δ is the dependent parameter. We determine δ so that the volume constraint given in Equation 24 is satisfied. Based on the error measures we found in the Section 3.1 we set $\epsilon_d = 4\ mm$ so that the error margin would be large enough to take into account the $\epsilon(t)\ \forall t$ and $\epsilon_v(t)\ \forall v$.

As in the previous section we carry our analysis for the images of the 8 different tumors (consisting 4 different growth parameter sets at 2 different locations) taken at different acquisition times. The comparison between the constant and

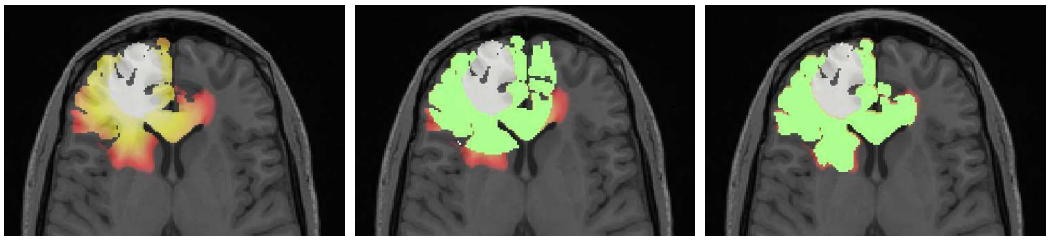

(a) Tumor distribution (b) Constant margin (c) Variable margin

Fig. 8. The proposed variable irradiation region construction takes into account the growth dynamics of the tumor. Figure shows the two irradiation margin construction approaches and the synthetic tumor cell distribution they aim to target. Figure (a) cell distribution of the synthetic tumor. The white region is the visible part while the colored region is the infiltration not visible in the image. Figures (b) and (c) show constant and variable irradiation regions overlaid on the tumor distribution respectively. Green regions represent the areas to be irradiated. For the synthetic tumor the variable margin better covers the extent of the infiltration therefore provides a better targetting.

the variable irradiation margins are given in Figures 9 and 10, where R and Vol graphs are plotted.

Analyzing the results given in Figures 9 and 10 we notice that including the tumor growth dynamics in tailoring the irradiation margin greatly improves the spatial targeting of the therapy in the case of synthetically grown tumors. Observing these figures we see that for all the cases we experimented with, the R and Vol curves for the variable irradiation margin remains well below the curves for the constant margin, with a great difference in most cases. For example 350 days after the detection of the tumor the difference in number of tumor cells targeted between the two approaches can go up to 5×10^8 $Cells$. On the other hand the difference in volume of healthy tissue targeted between the constant and variable margin approaches goes up to 13 cm^3. These values suggest that, assuming tumor growth tendencies is well captured by reaction-diffusion models, the variable irradiation margin is more efficient in targeting tumor cells and irradiating less healthy brain tissue. Moreover, we can state the followings after observing the graphs:

- Looking at the R graphs for the tumor in the parietal lobe we notice that the difference between the constant and the variable margins in targeting tumor cells increases as time passes. For example in the "low $d_{w,g}/\rho$" case, the difference between targeted tumor cells rises from 1×10^7 to 3×10^7 from the image taken at day 0 to the one taken at day 350. This suggests that as time passes tumor cells diffuse further and the anisotropy in the form of the tumor distribution increases. As a result, this amplifies the difference between the variable and the constant margins. On the other hand, we do not clearly observe such an increase for the tumor in the frontal lobe. This is due to the different tissue composition in that area. This demonstrates

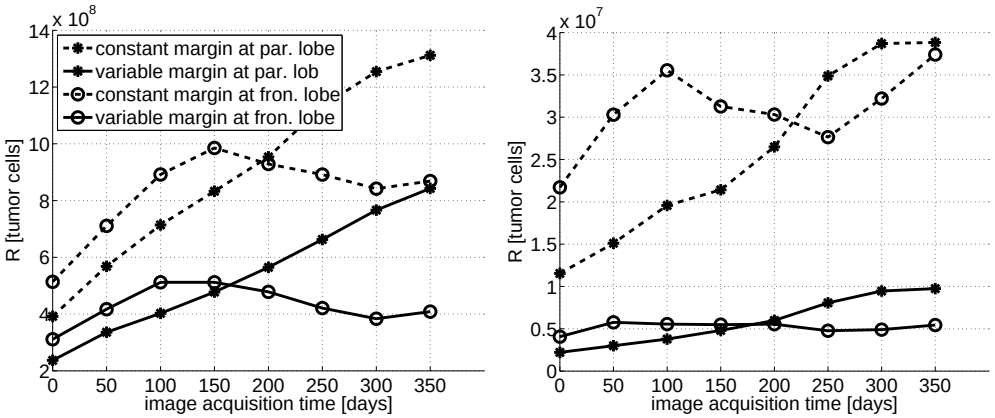

(a) high $d_{w,g}/\rho$

(b) low $d_{w,g}/\rho$

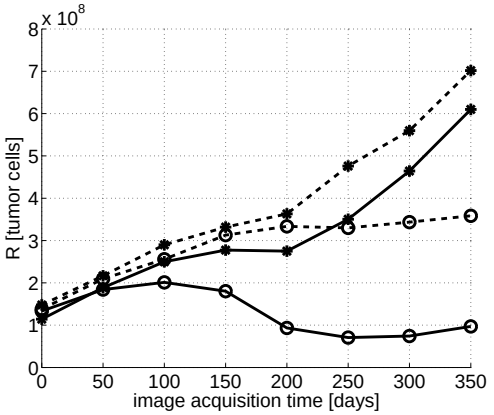

(c) lower anisotropy

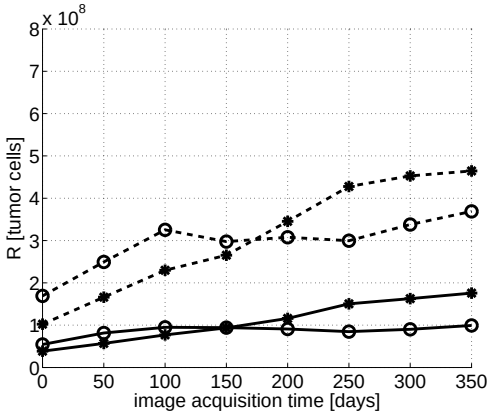

(d) higher anisotropy

Fig. 9. R vs. image acquisition time (after detection) plots for the synthetic tumors. We note that for figures (a) and (b) different y-axis scales are used for better visualization. In (a) values go up to 14×10^8 and in (b) they go up to 4×10^7. Results obtained for tumors with the same parameters but at different locations are plotted on the same graph. The variable irradiation margin targets more tumor cells than the constant margin (difference goes up to 5×10^8 cells). The plots demonstrates the possible higher efficiency of using variable irradiation margins in terms of targeting tumor cells.

the importance of the underlying tissue structures.

- Comparing Figures 9 (a) and (b) (note the scale difference in the y-axes), we observe that both schemes are more successful in targeting tumor cells when the diffusion is less and the proliferation is higher (the growth is more proliferation dominated). This is due to the fact that with higher diffusion, tumor cells infiltrate further away in the brain parenchyma creating a need for a larger irradiation margin. Moreover, as the tumor becomes more diffusive we observe that the difference between the two schemes in terms of tumor cells not targeted increases (the differences in Figure (a) are around 4×10^8 while in (b) they are around 3×10^7).
- Comparing Figures 9 (c) and (d), we see that the effect of increasing anisotropy

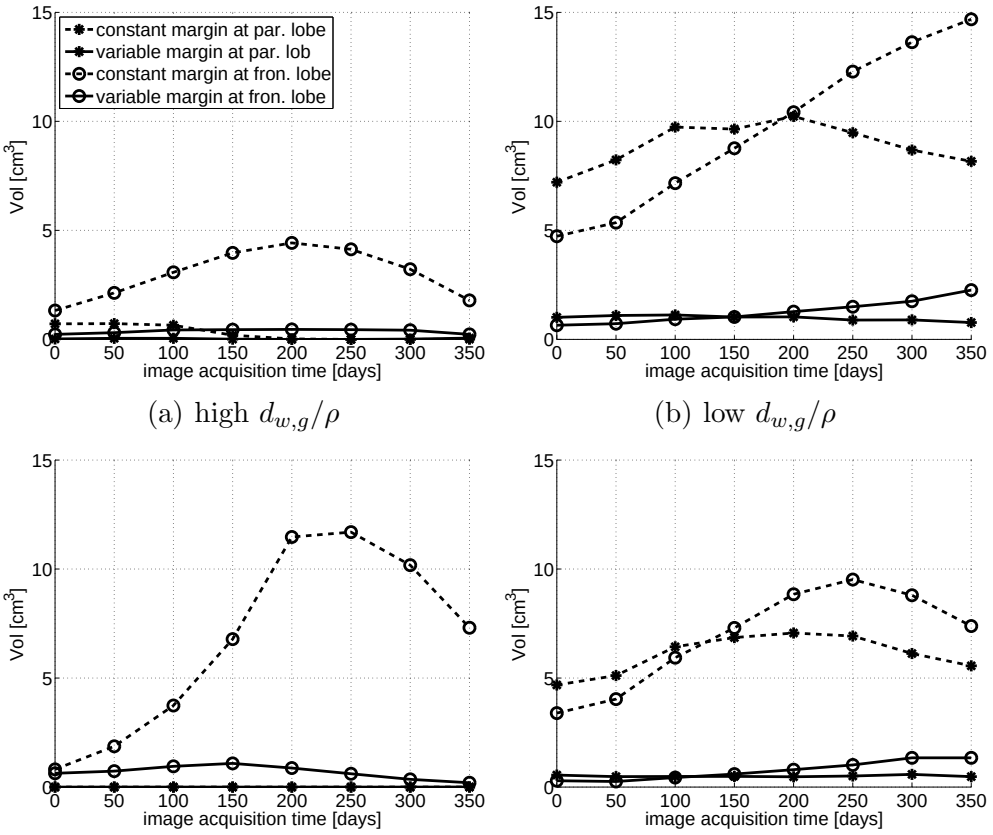

(a) high $d_{w,g}/\rho$ (b) low $d_{w,g}/\rho$

(c) lower anisotropy (d) higher anisotropy

Fig. 10. Vol vs. image acquisition time (after detection) plots for the synthetic tumors. Results obtained for tumors with the same parameters but at different locations are plotted on the same graph. The variable irradiation margin targets less healthy tissue than the constant margin(difference goes up to $13cm^3$). This demonstrates the possible higher efficiency of using variable irradiation margins in terms of saving healthy tissue.

depends on the location of the tumor. For the tumor in the parietal lobe we notice that when the anisotropy is higher the difference in number of tumor cells not targeted between the two schemes is much higher (in Figure (c) the maximum difference is around 1.2×10^8 while in Figure (d) it is around 3.0×10^8). This is as expected since variable irradiation margin takes into account the anisotropy while the constant one does not. On the other hand, we observe that for the tumor in the frontal lobe the difference between the two schemes is the same for low and high anisotropy. The reason for this is the fact that while constructing the variable irradiation margins we are taking into account the routes of invasion of the tumor especially the routes between the hemispheres. This becomes important for the tumors in the frontal lobe (see Figure 8) increasing the difference between the constant and the variable margins even in the case of isotropic tumors.

- Looking at Figures 10 (c) and (d) we observe the same trend as in the

previous item. For the tumor in the parietal lobe the difference in the volume of healthy tissue irradiated is greater in the higher anisotropy case. This is expected since as the anisotropy is lower the tumor grows "more" spherically and the difference between the variable and the constant margin decreases. For the tumor in the frontal lobe, the difference between the two schemes in irradiated healthy tissue is even higher for lower anisotropy. This is the potential benefit of taking into account the invasion routes of glioma cells.

- Comparing Figures 10(a) and (b) we observe that the difference between the two schemes is lower when the tumor is more diffusive. This is expected since there is less healthy tissue when the tumor infiltration covers a larger area. As a result the difference between schemes is less.
- Observing Figure 10(c) we see that no healthy tissue is irradiated in the parietal lobe. In this case, the high gray matter diffusion results in a large almost spherical infiltration extent. This extent is large enough to totally cover both of the margins proposed by the two strategies. As a result the volume of healthy tissue targeted is zero. A similar phenomenon is also observed for Figure 10(a). This time although the growth of the tumor is anisotropic, it is highly diffusive. This results in a large infiltration extent totally covering both of the irradiation margins. This phenomenon is not observed for the tumors in the frontal lobe due to the routes of invasion between the hemispheres. As mentioned above these routes play an important role in these cases.

4 Conclusion

In this work, we addressed the problem of limited tumor visualization of medical images through mathematical tumor growth modeling. We proposed a novel formulation which integrates macroscopic tumor growth models with medical images to extrapolate the low density infiltration regions of gliomas starting from the visible part of the tumor. In deriving the proposed formulation, we started from the well known reaction-diffusion models assuming that the growth dynamics of gliomas are well captured by this type of modeling. We then used asymptotic approximations of reaction-diffusion models to formulate the proposed solution. The resulting formulation in a sense, complements the imaging process and provides a larger view of the extent of the tumor infiltration. The proposed extrapolation method can also be applied to other applications which are modeled by partial differential equations which bear traveling wave solutions (e.g. wound healing, cardiac modeling).

In the Section 3, we performed two types of experiments evaluating the proposed extrapolation method. First, we showed that for the synthetic tumors, the estimation of the tumor cell density distribution beyond the visible part constructed with the proposed method remains within the vicinity of 1-2 vox-

els of the actual cell density distribution. This approximation can naturally be improved by including the effect of tumor fronts curvature and convergence characteristics of the F-KPP equation with the expense of increasing complexity and loosing generality.

In the second part of Section 3 we demonstrated the significance of using the proposed extrapolation scheme for radiotherapy. We constructed variable irradiation regions, which take into account the possible infiltration extents of gliomas, and compared them to the constant margins used conventionally in clinical practice. The geometrical comparisons demonstrate that the proposed method has the potential to target more tumor cells while harming less healthy brain tissue. This suggests the possible higher efficiency we can obtain in radiation therapy by using irradiation margins taking into account the growth dynamics. In order to better understand the effect of the variable margins accurate therapy simulations should be carried on.

One of the most important assumptions we made in this work was that the tumor growth dynamics are well captured by the reaction-diffusion type models as proposed in different works such as [40,18,8]. These models cover the general tendencies in tumor growth such as macroscopic heterogeneity and anisotropy of tumor growth and provide a good match with clinical cases [42]. In this work the choice of modeling assumption is based on our concern in solving the mentioned problem using the information available in the current clinical practice. Reaction-diffusion models have few parameters which can be directly related to the information available in the medical images. Therefore, the models can be adapted to specific patient cases [23]. Although reaction-diffusion models lack in including microscopic spatio-temporal factors affecting the growth process, this problem can be overcome as more types images become available in the clinical setting. One can imagine that when high resolution metabolical images become available, which would allow us to visualize different integrins and enzymes for each patient, then the proposed formulation can be adapted such that it takes into account different spatio-temporal effects yielding a more realistic prediction of the extent of tumor infiltration. One other modeling point we did not take into account in this work is the mass effect of the tumor. The proposed method uses the patient image and solves static problem. Therefore, the deformation caused by the tumor's mass effect is taken into account in extrapolating the infiltration extents. Moreover, since the extrapolation method uses the patient DTI, the tumor's effect on the fiber structure is also taken into account implicitly. However, in this work as a first attempt we ignored the coupling between the cell density distribution and the mass effect. This remains as a future work for further improvements on the method.

The results and experiments we present in this work are all synthetic cases. In order to understand the real benefits of the formulation proposed in this work,

evaluations with patient cases and clinical validation should be performed. We envision two types of validations to be done. The first one is the *in-vivo* and *in-vitro* validation of the proposed extent of the tumor infiltration. Through microscopic investigations of post-mortem brain slices or animal models we can determine the real tumor cell distribution in the brain tissue. The comparison of this distribution with the extrapolated one would let us understand how close we can get to the real infiltration margin using the proposed method. As the imaging technologies improve we can also envision to use the MR Spectroscopy for the validation, which is harder to use at the moment due to resolution issues. After these first set of validations, clinical validations should also be performed to understand whether adapting the irradiation margins of the radiotherapy to the extrapolated infiltration extent of tumor is beneficial or not. Such an adaptation may suggest critical structures to be irradiated while this may turn out to be harmful for the patient.

References

[1] R. Araujo, D. McElwain, A history of the study of solid tumour growth: the contribution of mathematical modelling, Bulleting of Mathematical Biology 66.

[2] D. Aronson, H. Weinberger, Multidimensional nonlinear diffusion arising in population genetics, Advances in Mathematics 30 (1978) 33–76.

[3] C. Athale, T. Deisboeck, The effects of EGF-receptor density on multiscale tumor growth patterns, J. Theor. Biol. 238 (2006) 771–779.

[4] C. Breward, H. Byrne, C. Lewis, A multiphase model describing vascular tumour growth, Bull. Math. Biol. 01.

[5] P. Burger, P. Dubois, S. Schold, K. Smith, G. Odom, D. Crafts, F. Giangaspero, Computerized tomographic and pathologic studies of the untreated, quiescent, and recurrent glioblastoma multiforme, J. Neurosurg. 58 (1983) 159–169.

[6] H. Byrne, M. Owen, T. Alarcon, J. Murphy, P. Maini, Modelling the response of vascular tumours to chemotherapy: a multiscale approach, Mathematical Models and Methods in Applied Sciences 16 (7S) (2006) 1219–1241.

[7] H. Byrne, L. Preziosi, Modelling solid tumour growth using the theory of mixtures, Math Med Biol 20 (2003) 341–366.

[8] O. Clatz, M. Sermesant, P. Bondiau, H. Delingette, S. Warfield, G. Malandain, N. Ayache, Realistic simulation of the 3d growth of brain tumors in mr images coupling diffusion with biomechanical deformation, IEEE T.M.I. 24 (10) (2005) 1334–1346.

[9] V. Cristini, J. Lowengrub, Q. Nie, Nonlinear simulation of tumor growth, Journal of Math. Biol. 46 (2003) 191–224.

[10] G. Cruywagen, D. Woodward, P. Tracqui, G. Bartoo, J. Murray, E. Alvord, The modelling of diffusive tumours, J. Biol. Systems 3.

[11] D. Drasdo, S. Höhme, A single-cell-based model of tumor growth *in vitro*: monolayers and spheroids, Phys. Biol. 2 (2005) 133–147.

[12] R. Fisher, The wave of advance of advantegous genes, Ann. Eug. 7 (1937) 355–369.

[13] H. Frieboes, J. Lowengrub, S. Wise, X. Zheng, P. Macklin, E. Bearer, V. Cristini, Computer simulation of glioma growth and morphology, NeuroImage 37 (2007) S59–S70.

[14] A. Giese, L. Kluwe, B. Laube, H. Meissner, M. Berens, M. Westphal, Migration of human glioma cells on myelin, Neurosurgery 38 (4) (1996) 755–764.

[15] B. Gompertz, On the nature of the function expressive of the law of human mortality, and on a new mode of determining the value of life contingencies, Phil. Trans. Royal Society of London 115 (1825) 513–585.

[16] C. Hogea, C. Davatzikos, G. Biros, Modeling glioma growth and mass effect in 3d mr images of the brain, in: Lec. Notes Comp. Sci. 4791, Medical Image Computing and Computer-Assisted Intervention – MICCAI 2007, 2007.

[17] C. Hogea, B. Murray, J. Sethian, Simulating complex tumor dynamics from avascular to vascular growth using a general level-set method, Journal of Mathematical Biology 53 (1) (2006) 86–134.

[18] S. Jbabdi, E. Mandonnet, H. Duffau, L. Capelle, K. Swanson, M. Pélégrini-Issac, R. Guillevin, H. Benali, Simulation of anisotropic growth of low-grade gliomas using diffusion tensor imaging, Magnetic Reson. in Med. 54 (3) (2005) 616–624.

[19] A. Kansal, S. Torquato, G. H. IV, E. Chiocca, T. Deisboeck, Simulated brain tumor growth dynamics using a three-dimensional cellular automaton, Journal of Theoretical Biology 203 (2000) 367–382.

[20] G. Kantor, H. Loiseau, A. Vital, J. Mazeron, Descriptions of GTV and CTV for radiation therapy of adult glioma, Cancer Radiother. 5 (5) (2001) 571–580.

[21] N. Kaspari, B. Michaelis, G. Gademann, Using an artificial neural network to define the planning target volume in radiotherapy, Journal of Medical Systems 21 (1997) 389–401.

[22] E. Konukoglu, O. Clatz, P.-Y. Bondiau, H. Delingette, N. Ayache, Extrapolating tumor invasion margins for physiologically determined radiotherapy regions, in: Proc. of the 9th International Conference on Medical Image Computing and Computer Assisted Intervention (MICCAI'06), Part I, No. 4190 in LNCS, 2006.

[23] E. Konukoglu, O. Clatz, B. Menze, M.-A. Weber, B. Stieltjes, E. Mandonnet, H. Delingette, N. Ayache, Image guided personalization of reaction-diffusion type tumor growth models using modified anisotropic eikonal equations, IEEE Tran. Med. Imag. In press 2009.

[24] E. Konukoglu, M. Sermesant, O. Clatz, J.-M. Peyrat, H. Delingette, N. Ayache, A recursive anisotropic fast marching approach to reaction diffusion equation: Application to tumor growth modeling, in: IPMI 2007, LNCS 4584, 2007.

[25] P. Maini, D. McElwain, D. Leavesley, Traveling wave model to interpret a wound-healing cell migration assay for human peritoneal mesothelial cells, Tissue Eng. 10.

[26] A. Mohamed, C. Davatzikos, Finite element modeling of brain tumor mass-effect from 3d medical images, in: Lec. Notes Comp. Sci 3749, MICCAI, 2005.

[27] J. Murray, Mathematical Biology, Springer-Verlag, 2002.

[28] A. Patel, E. Gawlinski, S. Lemieux, R. Gatenby, A cellular automaton model of early tumor growth and invasion, Journal of Theo. Biol. 213 (3) (2001) 315–331.

[29] S. Price, N. Burnet, T. Donovan, H. Green, A. P. na, N. Antoun, J. Pickard, T. Carpenter, J. Gillard, Diffusion tensor imaging of brain tumours at 3t: A potential tool for assessing white matter tract invasion?, Clinical Radiology 58 (2003) 455–462.

[30] J. Qian, Y. Zhang, H. Zhao, A fast sweeping method for static convex hamilton-jacobi equations, UCLA Comp. and App. Math. Reports 06-37.

[31] S. Sanga, H. Frieboes, X. Zheng, R. Gatenby, E. Bearer, V. Cristini, Predictive oncology: A review of multidisciplinary, multiscale in silico modeling linking phenotype, morphology and growth, NeuroImage 37 (2007) S120–S134.

[32] R. Seither, B. Jose, K. Paris, R. Lindberg, W. Spanos, Results of irradiation in patients with high-grade gliomas evaluated by magnetic resonance imaging, Am. J. Clin. Oncol. 18 (1995) 297–299.

[33] J. Sethian, Level set methods and fast marching methods: Evolving interfaces in computational geometry, fluid mechanics, computer vision, and materials science, Cambridge University Press, 1999.

[34] J. Sethian, A. Vladimirsky, Ordered upwind methods for static hamilton-jacobi equations: theory and algorithms, SIAM J. Numer. Anal. 41 (1) (2003) 325–363.

[35] G. Stamatakos, V. Antipas, N. Uzunoglu, A spatiotemporal, patient individualized simulation model of solid tumor response to chemotherapy in vivo: The paradigm of glioblastoma multiforme treated by temozolomide, IEEE Tran. Bio. Med. Eng. 53 (8) (2006) 1467–1477.

[36] G. Stamatakos, V. Antipas, N. Uzunoglu, R. Dale, A four-dimensional computer simulation model of the in-vivo response to radiotherapy of glioblastoma multiforme: studies on the effect of clonogenic cell density, Brit. J. Rad. 79 (2006) 389–400.

[37] A. Stein, T. Demuth, D. Mobley, M. Berens, L. Sander, A mathematical model of glioblastoma tumor spheroid invasion in a three-dimensional in vitro experiment, Biophys. J. 92 (2007) 356–365.

[38] W. Strauss, Partial differential equations: An introduction, Wiley and Sons, New York, 1992.

[39] K. Swanson, E. Alvord, J. Murray, A quantitative model for differential motility of gliomas in grey and white matter, Cell Prolif. 33 (5) (2000) 317–329.

[40] K. Swanson, E. Alvord, J. Murray, Virtual brain tumours (gliomas) enhance the reality of medical imaging and highlight inadequacies of current therapy, British Journal of Cancer 86 (2002) 14–18.

[41] K. Swanson, E. Alvord, J. Murray, Dynamics of a model for brain tumors reveals a small window for therapeutic intervention, Discrete and Continous Dynamical Systems-Series B 4 (1) (2004) 289–295.

[42] K. Swanson, R. Rostomily, E. Alvord, A mathematical modelling tool for predicting survival of individual patients following resection of glioblastoma: a proof of principle, British Journal of Cancer 98 (2008) 113–119.

[43] M. Taylor, Partial differential equations 1: Basic Theory, Springer, 1996.

[44] M. Tovi, Mr imaging in cerebral gliomas analysis of tumour tissue components, Acta Radiol. Suppl. 384 (1993) 1–24.

[45] P. Tracqui, G. Cruywagen, D. Woodward, G. Bartoo, J. Murray, E. Alvord, A mathematical model of glioma growth: the effect of chemotherapy on spatio-temporal growth, Cell Proliferation 28 (1) (1995) 17–31.

[46] W. S. U. Ebert, Front propagation into unstable states: universal algebraic convergence towards uniformly translating pulled fronts, Physica D: Nonlinear Phenomena 146.

[47] P.-F. Verhulst, Recherches matheématiques sur la loi d'accroissement de la population, Nouveau mémoires de l'Académie Royale des Sciences et Belles-Lettres de Bruxelles 18 (1845) 1–41.

[48] M. Watanabe, R. Tanaka, N. Takeda, K. Wakabayashi, H. Takahashi, Correlation of computed tomography with the histopathology of primary malignant lymphoma of the brain, Neuroradiology 34 (1992) 36–42.

[49] A. Zizzari, B. Michaelis, G. Gademann, Simulation and modeling of brain tumors in computer-assisted radiotherapy, in: Proc. IASTED Conf. Applied Simulation and Modelling, 2004.

APPENDIX

A Derivation of the Extrapolation Integral

When we linearize the Equation 7 around the point $\overline{\xi}^*, u^*$ we get

$$D_{\mathbf{n}}\frac{d^2u}{d\overline{\xi}^2} + 2\sqrt{\rho D_{\mathbf{n}}}\frac{du}{d\overline{\xi}} + \rho u(1-u^*) = 0. \tag{A.1}$$

Equation A.1 can be solved analytically and the solution has the form

$$u_{\overline{\xi}^*}(\overline{\xi}) = Be^{-\lambda(1+\sqrt{u^*})\overline{\xi}} + Ae^{-\lambda(1-\sqrt{u^*})\overline{\xi}} \tag{A.2}$$

$$\lambda = \sqrt{\frac{\rho}{D_{\mathbf{n}}}}, \tag{A.3}$$

where A and B are integration constants and $u_{\overline{\xi}^*}$ is the local solution around $\overline{\xi}^*$. Due to the smooth properties of the reaction-diffusion equations this solution can be used as an approximation for the solution of Equation 7 in a small neighborhood around $\overline{\xi}^*$ [43]. Then using the u values found on the boundary of this neighborhood one can construct the approximations for the adjacent neighborhoods and cover the whole domain like this. By constructing and combining these local approximations in a successive manner, we reconstruct the shape of the traveling wave $u(\overline{\xi})$ starting from the known point $u(\overline{\xi^*}) = u^*$. This idea is demonstrated in Figure A.1.

In order to obtain the relationship between the two constants A and B we use the fact that $u = 0.5$, the origin of the moving frame $\overline{\xi}$, is an inflection point of the traveling wave [27]. Therefore, the second derivative of u at $u = 0.5$ should be zero. When we impose this to the local solution around u^* which is close to $u = 0.5$ we get

$$\frac{A}{B} = \frac{(1+\sqrt{u^*})^2}{(1-\sqrt{u^*})^2}. \tag{A.4}$$

For values of u^* close to 0.5 this ratio remains well over 20. The contribution of $Be^{-\lambda(1+\sqrt{u^*})\overline{\xi}}$ is much smaller than the other part. Therefore, we ignore this part of the solution given in Equation A.2. As a result the local approximation $\tilde{u}_{\overline{\xi}^*}$ of the tumor profile around u^* can be given as

$$u_{\overline{\xi}^*}(\mathbf{x},t) \approx \tilde{u}_{\overline{\xi}^*}(\mathbf{x}) = \tilde{u}_{\overline{\xi}^*}(\overline{\xi}) = Ae^{-\lambda\overline{\xi}(1-\sqrt{u^*})} \quad \text{for} \quad \lambda = \sqrt{\rho/D_{\mathbf{n}}}. \tag{A.5}$$

We notice that the value of the integration constant A depends on the value of $\overline{\xi}$. The value of $\overline{\xi}$ at a point corresponds to its distance from the inflection point of the traveling wave, which is at $u = 0.5$ (see Figure 2(a)). From the

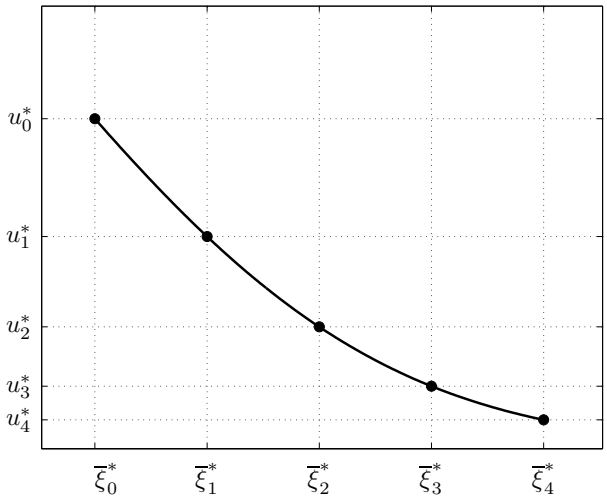

Fig. A.1. The shape of the traveling wave can be reconstructed starting from one known point and building local linear approximations to the reaction-diffusion equation with nonlinear reaction term. If the known point is $u(\overline{\xi}_0^*) = u_0^*$) then we can use the local linear approximation at this point to find the value $u(\overline{\xi}_1^*) = u_1^*$. Then using the linear approximation at $\overline{\xi}_1^*$ we can find the value u_2^* and the reconstruction process goes on like this.

images however, we can observe the regions where tumor cell density is greater than u_0. Therefore, we do not have access to the value of $\overline{\xi}$ at a point. For each local approximation this problem can be solved easily. For a point $\overline{\xi} = \overline{\xi}^* + \Delta\overline{\xi}$ we can write

$$\tilde{u}_{\overline{\xi}^*}(\overline{\xi}^* + \Delta\overline{\xi}) = Ae^{-\lambda(1-\sqrt{u^*})(\overline{\xi}^*+\Delta\overline{\xi})} \tag{A.6}$$

$$= Ae^{-\lambda(1-\sqrt{u^*})\overline{\xi}^*}e^{-\lambda(1-\sqrt{u^*})\Delta\overline{\xi}} \tag{A.7}$$

$$= u^*e^{-\lambda(1-\sqrt{u^*})\Delta\overline{\xi}}, \tag{A.8}$$

where $\Delta\overline{\xi}$ is a small distance since we remain close to the point u^*. Using ξ variable instead of the $\Delta\overline{\xi}$ we obtain our final local approximation for the form of the tumor profile (traveling wave)

$$\tilde{u}_{\overline{\xi}^*} = u^*e^{-\lambda(1-\sqrt{u^*})\xi} \quad \text{for} \quad \lambda = \sqrt{\rho/\mathbf{n}'D\mathbf{n}}. \tag{A.9}$$

We note that in the local neighborhood of $(\overline{\xi}^*, u^*)$ this solution can be written as the integral

$$\tilde{u}_{\overline{\xi}^*} = \int_0^{\xi} -\lambda(1-\sqrt{u^*})\tilde{u}_{\overline{\xi}^*}d\varphi \quad \text{with} \quad \tilde{u}_{\overline{\xi}^*}(0) = u^*. \tag{A.10}$$

When we take small enough neighborhoods around each u^*, in the limit, we replace u^* in the square root with $\tilde{u}_{\overline{\xi}^*}$. Here we assume that in such a small neighborhood $\tilde{u}_{\overline{\xi}^*}$ values will be close to u^*. Considering the smoothness of

the reaction-diffusion equations this approximation becomes valid [43]. With this approximation the local solution given by the integral becomes

$$\tilde{u}_{\overline{\xi}^*} = \int_0^{\xi} -\lambda(1 - \sqrt{\tilde{u}_{\overline{\xi}^*}})\tilde{u}_{\overline{\xi}^*} d\varphi \quad \text{with} \quad \tilde{u}_{\overline{\xi}^*}(0) = u^*. \tag{A.11}$$

Combining these local solutions in different neighborhoods using this integral form, we obtain the global approximation for the form of the traveling wave

$$\begin{aligned} \tilde{u}(\mathbf{x}) &= \int_0^{x} -\lambda(1 - \sqrt{\tilde{u}})\tilde{u} d\xi \quad \text{with} \quad \tilde{u}(0) = u_0, \\ \lambda &= \frac{\sqrt{\rho}}{\sqrt{\mathbf{n}' D \mathbf{n}}}. \end{aligned} \tag{A.12}$$

where x is the distance of the point $\mathbf{x}$ from the known point $u = u_0$.

B Applying the Method of Reflection on the Nonlinear PDE

The method of reflection is used to construct solutions of linear partial differential equations such as the diffusion equation in finite domains, [38]. It uses the solution under no boundary condition, reflects it with respect to the boundary and superpose these two, relying on the linearity of the equation. In the case of the nonlinear reaction diffusion equation we cannot superpose two different solutions of the system. In order to apply the method of reflection we make certain assumptions. Let $u^{(1)}$ and $u^{(2)}$ both satisfy the nonlinear equation

$$u_t = \nabla \cdot (D \nabla u) + \rho u(1 - u). \tag{B.1}$$

When we superpose the two solutions and plug it in Equation B.1 we get

$$\begin{aligned} (u^{(1)} + u^{(2)})_t &= \nabla \cdot (D \nabla (u^{(1)} + u^{(2)})) \\ &\quad + \rho(u^{(1)} + u^{(2)})(1 - u^{(1)} - u^{(2)}) \qquad \text{(B.2)} \\ u_t^{(1)} + u_t^{(2)} &= \nabla \cdot (D \nabla u^{(1)}) + \nabla \cdot (D \nabla u^{(2)}) \\ &\quad + \rho u^{(1)}(1 - u^{(1)}) + \rho u^{(2)}(1 - u^{(2)}) - 2\rho u^{(1)} u^{(2)}. \qquad \text{(B.3)} \end{aligned}$$

We see that the superposition of the two solutions do not satisfy the equation due to the nonlinearity. However, in this work we are interested in low values of u since we try to extrapolate the tumor cell density distribution below some threshold u_0. Therefore, the values of $u^{(1)}$ and $u^{(2)}$ are low. Based on this, we assume that

$$\frac{(1 - u^{(1)})}{u^{(2)}} >> 1 \quad \text{and} \quad \frac{(1 - u^{(2)})}{u^{(1)}} >> 1. \tag{B.4}$$

Using this assumption we can say that

$$\rho(1-u^{(1)})u^{(1)} >> \rho u^{(1)}u^{(2)} \quad \text{and} \quad \rho(1-u^{(2)})u^{(2)} >> \rho u^{(1)}u^{(2)}. \tag{B.5}$$

Hence, we assume that the superposition of two solutions satisfy the nonlinear reaction-diffusion equation for low values of u.

C Derivation of $\mathbf{u_{ref}}$

In order to derive $\mathbf{u_{ref}}$, let us assume that we have a homogeneous and anisotropic media characterized by the diffusion tensor D. Also let the visible tumor's boundary be a plane with the normal $\mathbf{n}$. In this case $\tilde{u}_{nb}$ and $\tilde{u}_{ref}$ can be written in their integral forms like Equation 11. These integrals are given as:

$$\begin{aligned}
\tilde{u} &= \tilde{u}_{nb} + \tilde{u}_{ref}, \\
\tilde{u}_{nb}(\mathbf{x}) &= \int_0^x -\lambda_{nb}(1-\sqrt{\tilde{u}_{nb}})\tilde{u}_{nb}d\xi \quad \text{with} \quad \tilde{u}_{nb}(\Gamma) = \mathbf{u_{nb}}, \quad \xi(\Gamma) = 0 \quad \text{(C.1)} \\
\tilde{u}_{ref}(\mathbf{x}) &= \int_0^x -\lambda_{ref}(1-\sqrt{\tilde{u}_{ref}})\tilde{u}_{ref}d\widehat{\xi} \quad \text{with} \quad \tilde{u}_{ref}(\partial\Omega) = \mathbf{u_{ref}}, \quad \widehat{\xi}(\partial\Omega) = 0 \quad \text{(C.2)} \\
\lambda_{nb} &= \sqrt{\frac{\rho}{\mathbf{n}^T D\mathbf{n}}}, \\
\lambda_{ref} &= \sqrt{\frac{\rho}{\mathbf{n}_{\partial\Omega}^T D\mathbf{n}_{\partial\Omega}}}, \\
\xi &= \mathbf{n}^T\mathbf{x} - ct, \\
\widehat{\xi} &= \mathbf{n}_{\partial\Omega}^T\mathbf{x} - ct,
\end{aligned}$$

where $\mathbf{n}$ is the gradient direction of $\tilde{u}_{nb}$, $\mathbf{n}_{\partial\Omega}$ is the normal to the boundary (which by construction coincides with the gradient direction of $\tilde{u}_{ref}$ at the boundary) and x is the distance of point $\mathbf{x}$ to the tumor delineation. Notice that due to the anisotropy in the diffusion tensor λ_{nb} and λ_{ref} differ. As suggested by the method of reflection the $\tilde{u}_{ref}$ decreases in the opposite direction of u_{nb} so to satisfy the no-flux boundary condition, i.e. $\mathbf{n}_{\partial\Omega}^T\mathbf{n} < 0$.

Since we know $\mathbf{u_{nb}}$ (this is set before $\mathbf{u_{ref}}$ in the iterative scheme), we start from the tumor delineation Γ and construct $\tilde{u}_{nb}$ as we sweep the domain outwards. Based on the knowledge of $\tilde{u}_{nb}|_{\partial\Omega}$ we set $\mathbf{u_{ref}}$ so to satisfy the boundary condition which is given as:

$$\mathbf{n}_{\partial\Omega}^T D\nabla\tilde{u}|_{\partial\Omega} = 0 \tag{C.3}$$

Using this condition, we find the relation between $\tilde{u}_{nb}$ and $\tilde{u}_{ref}$ at each bound-

ary point separately since every point on the boundary acts as a cell reflector. Placing the integral formulations of $\tilde{u}_{nb}$ and $\tilde{u}_{ref}$, for $\tilde{u}$ we obtain

$$\tilde{u} = \int_0^x -\lambda_{nb}(1-\sqrt{\tilde{u}_{nb}})\tilde{u}_{nb}d\xi + \int_0^x -\lambda_{ref}(1-\sqrt{\tilde{u}_{ref}})\tilde{u}_{ref}d\widehat{\xi}. \tag{C.4}$$

Using the fundamental theorem of calculus we can compute the gradient of $\tilde{u}$ at any point $\mathbf{p} \in \partial\Omega$

$$\nabla\tilde{u}|_{\mathbf{p}} = (\nabla\tilde{u}_{nb} + \nabla\tilde{u}_{ref})_{\mathbf{p}} \tag{C.5}$$

$$\nabla\tilde{u}|_{\mathbf{p}} = -\lambda_{nb}(1-\sqrt{\tilde{u}_{nb}})\tilde{u}_{nb}|_{\mathbf{p}}\mathbf{n} - \lambda_{ref}(1-\sqrt{\mathbf{u_{ref}}})\mathbf{u_{ref}}|_{\mathbf{p}}\mathbf{n}_{\partial\Omega} \tag{C.6}$$

Forcing the boundary condition given in Equation C.3 we obtain the relation we are looking for the points on the boundary

$$\begin{aligned}&(1-\sqrt{\mathbf{u_{ref}}(\mathbf{p})})\mathbf{u_{ref}}(\mathbf{p}) = \\ &\quad -\frac{\mathbf{n}_\Omega^T D\mathbf{n}}{\sqrt{\mathbf{n}^T D\mathbf{n}}\sqrt{\mathbf{n}_\Omega^T D\mathbf{n}_\Omega}}(1-\sqrt{\tilde{u}_{nb}(\mathbf{p})})\tilde{u}_{nb}(\mathbf{p}),\ \text{for } \mathbf{p}\in\partial\Omega\end{aligned} \tag{C.7}$$

Therefore, for each point on the boundary we can find $\mathbf{u_{ref}}$ by solving the 4^{th} order polynomial given by the Equation above. However, this is rather costly, especially if we consider that we will solve this equation for many different points on a 3D boundary. Therefore, we make the approximation

$$\frac{(1-\sqrt{\mathbf{u_{ref}}(\mathbf{p})})\mathbf{u_{ref}}(\mathbf{p})}{(1-\sqrt{\tilde{u}_{nb}(\mathbf{p})})\tilde{u}_{nb}(\mathbf{p})} \approx \frac{\mathbf{u_{ref}}(\mathbf{p})}{\tilde{u}_{nb}(\mathbf{p})}. \tag{C.8}$$

When the $\tilde{u}_{nb}$ values are low this approximation is pretty close to the original solution. And since we expect low values (at least $\tilde{u} < 0.4$) on the boundary points the effect of this approximation on the overall solution would be small. As a result of this approximation we transform Equation C.7 into

$$\mathbf{u_{ref}}(\mathbf{p}) = -\frac{\mathbf{n}_\Omega^T D\mathbf{n}}{\sqrt{\mathbf{n}^T D\mathbf{n}}\sqrt{\mathbf{n}_\Omega^T D\mathbf{n}_\Omega}}\tilde{u}_{nb}(\mathbf{p}),\ \text{for } \mathbf{p}\in\partial\Omega \tag{C.9}$$

The $\mathbf{u_{ref}}$ is computed independently for each boundary point. Here we can repeat the same assumptions about coefficients being constant and tumor front being planar within a voxel. As a result the integral forms given in Equations C.1 and C.2 can be given by the gradient relationships given in Equations 18 and 19 respectively. The condition given in Equation C.9 is local it applies directly for the gradient relations as well.